Materials Advances

Accepted Manuscript

This article can be cited before page numbers have been issued, to do this please use: K. M. Kaky, M. I. Sayyed, K. A. Mahmoud, M.H.A. Mhareb, I. Abed Jawad and S. Kamath, *Mater. Adv.*, 2026, DOI: 10.1039/D6MA00313C.

ROYAL SOCIETY OF CHEMISTRY

rsc.li/materials-advances

View Article Online
DOI: 10.1039/D6MA00313C

Structural, Optical, Mechanical, and Gamma-Ray Shielding Properties of Er_2O_3-Doped Germano-Tellurite-Borate Glasses

Kawa M. Kaky [1,*], M.I. Sayyed [2,3], K. A. Mahmoud [4,5], M.H.A. Mhareb [6,7], Israa Abed Jawad[1], Sudha D Kamath[8,*]

[1]*Al-Nisour University College, Baghdad, Iraq*
[2]*Department of Physics, Faculty of Science, Isra University, Amman, Jordan*
[3]*Department of Physics and Technical Sciences, Western Caspian University, Baku, Azerbaijan*
[4]*Ural Federal University, 19 Mira St, 620002, Yekaterinburg, Russia.*
[5] Department of Physics, Dogus University, Dudullu-Ümraniye, 34775 Istanbul, Türkiye
[6]*Department of Physics, College of Science, Imam Abdulrahman Bin Faisal University, P.O. Box 1982, Dammam, 31441, Saudi Arabia*
[7]*Basic and Applied Scientific Research Center, Imam Abdulrahman Bin Faisal University, P.O. Box 1982, Dammam, 31441, Saudi Arabia*
[8]*Department of Physics, Manipal Institute of Technology, Manipal Academy of Higher Education, Manipal, Karnataka, India*

Abstract

The study deals with fabrication of a new germano-tellurite-borate glass series for optical and gamma-ray shielding applications. The chemical formula 20 TeO_2 + 10 GeO_2 + (35-y) B_2O_3 + 35 MgO + y Er_2O_3 describes the fabricated germano-tellurite-borate glass series, where y takes values of 1.25, 2.5, 3.75, and 5 mol%. The X-ray diffractometer (XRD) was used to affirm the amorphous phase of the fabricated glasses. Furthermore, the impact of partial replacement of Er_2O_3 for B_2O_3 on the optical properties of the examined glasses was evaluated based on the UV-Vis absorption spectra, which is detected by a spectrophotometer along with a wavenumber varied from 200 to 1200 nm. The refractive index of the examined glasses increased from 2.620 to 2.270 when the Er_2O_3 increased from 1.25 to 5 mol%, respectively. Also, the impact of partial replacement of Er_2O_3 for B_2O_3 on the mechanical properties of the investigated glasses was evaluated based on Makishima and Mackenzie's theory. The increase in the Er_2O_3 content from 1.25 to 5 mol% enhances the hardness of the investigated glasses from 5.217 to 5.263 GPa, respectively. Additionally, the γ-ray protecting parameters were estimated using Monte Carlo simulation over the broad 0.0332–2.506 MeV energy interval. According to the acquired findings, the prepared samples' linear attenuation coefficient enhances by 54.94%, 11.09%, and

View Article Online
DOI: 10.1039/D6MA00313C

6.94%, respectively, at the 0.059, 0.511, and 2.506 MeV γ-ray energies as the Er_2O_3 increases over a concentration of 1.25–5 mol%.

Keywords: Erbium oxide (Er_2O_3) doping; Germano-tellurite-borate glass; Optical absorption spectra; Gamma-ray attenuation coefficient; Radiation shielding materials

***Corresponding author:** sudha.kamath@manipal.edu (S.D. Kamath).

1. **Introduction**

Researchers have recently become more interested in exploring improved glass systems for novel industrial and technological uses [1–5]. Due to attractive properties such as excellent optical transparency, high refractive index, low melting point, chemical durability, thermal stability, favorable electrical properties, and adequate radiation shielding properties, borotellurite glasses have gained considerable attention [6–9]. These fascinating properties make borotellurite glasses promising materials for different applications, including radiation shielding materials, optical fibers and waveguides, non-linear optical devices, photonic devices, luminescent materials, biomedical applications, memory devices, and data storage [10–15].

TeO_2 cannot form glass under typical quenching situations unless an additional constituent is added. Tellurite glasses, hence, require the inclusion of secondary components like heavy metal oxides, and rare earth oxides. TeO_2 combined with additional components produces glasses that are durable and allow for the control of desired characteristics [3,16,17].

To improve the borotellurite glass network's density and effective atomic number, GeO_2 and Er_2O_3 are added. These advantageous characteristics led to the selection of GeO_2 and Er_2O_3 as additional components in our attempt to produce borotellurite glasses [18]. Traditionally, the widespread use of lead-based glasses has achieved gamma-ray radiation shielding from other ionizing, human-hazardous radiation. Due to their toxicity, lead-based glasses are not preferable

View Article Online
DOI: 10.1039/D6MA00313C

in radiation shielding applications, and thus the researchers are trying to develop free lead glasses for radiation shielding purposes.

The literature [19–24] highlights several efforts to replace lead-based glasses with lead-free alternatives or radiation-shielding glasses. The borotellurite glasses with HMO exhibit remarkable shielding ability equal to or exceeding that of different glass systems. Consequently, comprehending borotellurite-based glasses' shielding efficiency and their ability to attenuate ionizing radiation is essential for their application in radiation environments [25,26].

The Monte Carlo N-Particle Transport Code fifth version (MCNP5) is a simulation program developed by the Los Alamos National Laboratory, utilizing the mathematical technique of Monte Carlo simulation to solve the transport equation for studying radiation–material interactions. It can operate using many forms of radiation exposure, and in terms of radiation sources, it can utilize neutrons, photons, and electrons. MCNP serves as a functional instrument for evaluating radiation interaction characteristics in various mixes and compounds, facilitating shielding and energy absorption in human organs and tissues through the application of physics models for nuclear cross-sections and particle interaction libraries [27,28].

On the other hand, XCOM represents a useful software resource for the study of radiation shielding that can estimate glasses' (and other composites) mass attenuation coefficient (MAC) at different energy levels [29]. This software and other similar software (such as Phy-X software) support the simulation and experimental works by allowing researchers to define their materials using the composition and the density of the materials at certain energies [30].

The novelty of the current work is to fabricate a new germano-tellurite-borate glass series described by the chemical formula 20 TeO_2 + 10 GeO_2 + (35-y) B_2O_3 + 35 MgO + y $E_{r2}O_3$; y = 1.25, 2.5, 3.75, and 5 mol%. The influence of partial substitution of Er_2O_3 for B_2O_3 compounds

View Article Online
DOI: 10.1039/D6MA00313C

on the structural, optical, mechanical, and gamma-ray shielding capacity was examined using various experimental and theoretical methods.

2. Methodology

2.1. Samples fabrication

In the present case, a series of erbium oxide doped-germanate tellurite borate glass is fabricated based on the chemical formula of 20 TeO_2 + 10 GeO_2 + (35-y) B_2O_3 + 35 MgO + y Er_2O_3 with y values of 1.25, 2.5, 3.75, and 5 mol%. The high-purity chemicals were from established suppliers such as Sigma-Aldrich. The desired chemicals were weighed to prepare a 15 g patch using the molar proportion shown in **Table 1**. A plastic container that is labeled for each composition was prepared, and all chemicals involved in the desired glass samples were blended and mixed for 20 min so the homogeneous structure could be ensured. Er1, Er2, Er3, and Er4 powders were then poured into a crucible made of high alumina and placed for 20 min in a 1100°C electric muffle furnace for melting. The Er1, Er2, Er3, and Er4 glass molten was poured on a pre-heated stainless-steel disc, with the samples then cooling to room temperature gradually to negate a sudden high change of the temperature that leads to cracking. To release any internal stress in the glass samples, 5 h of annealing was conducted in another furnace at 350°C. The final Er1, Er2, Er3, and Er4 glass samples are presented in **Figure 1**, with further structural and optical characterizations carried out. The origin software was used to plot all figures in this manuscript.

The density (ρ, g/cm^3) of the fabricated Er glasses was measured according to Archimedes' principle in Eq. (1) [31,32].

$$\rho_{glass}\left(\frac{g}{cm^3}\right) = \frac{M_a}{(M_a - M_i)} \times \rho_{water} \quad (1)$$

View Article Online
DOI: 10.1039/D6MA00313C

In Eq. 1, M_a and M_i refer to the mass of fabricated Er glasses in air and immersed in water, while ρ_{glass} refers to the density of water (≈ 1 g/cm^3). The uncertinity in the measured densities for the examined samples ranges ±1.8%.

2.2. Glass characterization and optical properties

In the current work, Shimadzu XRD-6000 was used to measure the sample's X-ray diffraction (XRD) profiles in the 10–80◦ range to investigate the synthesized glasses' nature. The UV absorption spectra (3101, Japan; wavelength range: 200–1200 nm) were used to examine the optical characteristics. For band gap value determination, the absorption edge and the equation by Mott and Davis [33] were employed:

$$h\nu\alpha = A(h\nu - E_g)^n \quad (2)$$

where hv, A, and a respectively represent the photon energy, constant, and absorption coefficient,. Meanwhile, determination of the Urbach energy (E_U) used **Eq. 3**:

$$ln(\alpha) = ln(\alpha_0) + \frac{h\nu}{E_U} \quad (3)$$

In this case, a_o represents the corresponding constant. Based on E_g values, **Eq. 4** facilitated the determination of the refractive index (n):

$$\frac{(n^2-1)}{(n^2+2)} = 1 - \sqrt{\frac{E_g}{20}} \quad (4)$$

Several equations from our earlier study [34] were used to compute the following parameters: optical basicity (Λ), metallization, electron polarizability (α_o), and optical electronegativity (χ).

2.3. Mechanical properties

View Article Online
DOI: 10.1039/D6MA00313C

The Archimedes principle, as employed in [35], was used to quantify the density of fabricated samples. For the mechanical properties' evaluation, the study used the Makishima and Mackenzie (M-M) model [36]. The main model components, the packing density (V_t) and the dissociation energy (G_t), are presented in **Eqs. 5** and **6** [37]:

$$V_t = \sum_i \frac{V_i\, x_i}{V_m} \quad (5)$$

$$G_t = \sum_i x_i G_i \quad (6)$$

where V_m, G_i, x_i, and V_i represent the molar volume, dissociation energy, mole ratio, and oxide packing factor, respectively. Equations previously given were used to compute the remaining mechanical characteristics [38,39].

2.4. Calculation of the γ-ray shielding characteristics

The γ-ray shielding parameters' evaluation was performed based on the MCNP [40], through which the shielding parameters were evaluated by estimating the prepared Er glass samples' γ-photons in terms of the track length (TL). The simulation processes were performed so that virtually all known γ-ray energies in the 0.0332–2.506 MeV interval would be covered. For accurate simulated data, an input file with well-arranged geometry should be created. **Figure 2** presents the created geometry, which comprises numerous cards (e.g., cell, cutoff, importance, material, source definition, surface, and tally), under which the details of the geometry should be introduced. According to the generated input file, the cell is deemed the smallest building unit inside the geometry, which comprises many cells. Each cell has a definite cell number and density. The cell is also surrounded by many surfaces that are defined and described under the surface card section, such as the shape and dimensions surrounding each cell in the input file. For example, the external shielding cell comprising pure lead (density: 11.34 g/cm^3) is cylindrical,

View Article Online
DOI: 10.1039/D6MA00313C

filled with dry air, and has the following measurements: thickness: 5 cm, diameter: 25 cm, height: 35 cm. The individual's elemental chemical composition was added to the material card. Moreover, the tally used to estimate the TL is F4, with the cutoff card set up to cease interactions following 10^6 historical emissions. Further simplification was achieved by setting the PHY card to (PHYS: P 1 0 0 0), thus indicating the absence of coherent scattering, Bremsstrahlung, photoelectric interaction fluorescence, or binding effects in photon scattering greater than 1 MeV. Finally, the output file's relative error produced by the simulation process was in the ± 0.1 range. Next, the simulated TL according to **Eq. 7** was used for the simulated LAC evaluation.

Then, the obtained TL from the output file was employed for the determination of the prepared Er glasses' linear attenuation coefficient (LAC, cm^{-1}). **Eqs. (8-12)** facilitated evaluation of the γ-ray shielding parameters, including the MAC (cm^2/g), half-value layer (HVL, cm), thickness equivalent lead (D_{eq}, cm), and radiation protection efficiency (RPE, %) according to the LAC, I_o, and I_t values [41–43].

$$LAC\ (cm^{-1}) = \frac{1}{x}\ln\left(\frac{I_o}{I_t}\right) \quad (7)$$

$$MAC\left(\frac{cm^2}{g}\right) = \frac{LAC\ (cm^{-1})}{\rho\ (\frac{g}{cm^3})} \quad (8)$$

For the non-shielded radioactive source, I_o is the detected activity. Using a thickness x (cm) from the prepared Er glass, the I_o values reduced to be I_t.

The half value thickness (HVL, cm) is the thickness of the fabricated Er glasses that can reduce the Io photons by 50% (i.e., $I_t = 50\%I_o$). The HVLs are related to the LACs of the examined Er glass samples, as appears in Eq. 9.

$$HVL\ (cm) = \frac{\ln(2)}{LAC} \quad (9)$$

View Article Online
DOI: 10.1039/D6MA00313C

Next, the obtained LAC, I_o, and I_t values were employed for the radiation shielding parameters' evaluation, including the RPE (%), thickness equivalent lead (Δ_{eq}, cm), and the transmission factor (TF, %), according to Eqs. (10-12).

The thickness equivalent lead (Δ_{eq}, cm) represents the thickness of the Er glass sample that has shielding capacity equal to that of a 1 cm thickness of pure lead. The Δ_{eq} values depend mainly on the LAC of pure lead and fabricated glasses, as presented in Eq. (10).

$$\Delta_{eq}(cm) = \frac{\mathrm{LAC}_{lead} \times x_{lead}}{\mathrm{LAC}_{Er\ glasses}} \qquad (10)$$

The transmission factor (TF, %) represents the percentage of transmitted photons (I_t) relative to the initial number of photons (I_o). It can be calculated according to Eq. 11 [44,45].

$$TF\ (\%) = \frac{I_t}{I_o} = \ \times 100 \qquad (11)$$

The Radiation protection efficiency (RPE, %) describes the percentage of photons absorbed (I_a) within the Er glass layer relative to the initial photon (I_o) numbers. The RPEs can be calculated according to Eq. **12**, where the I_a photons are I_o-I_t photons.

$$RPE\ (\%) = \frac{I_a}{I_o} = \ \frac{(I_o - I_t)}{I_o} \ \times 100 \qquad (12)$$

3. Results and discussion

3.1. X-ray diffraction

The XRD results for all glass samples are presented in **Figure 3**, where at 28 and 50 degrees two broad bands can be seen. In terms of the glass system, a lack of long order is indicated by the peaks, meaning that the current sample's network is amorphous.

3.2. Optical properties

Evaluating and comprehending a glass system's optical properties is vital for using glass in different applications. Measuring the absorption spectra for any glass system is considered the first step in evaluating optical properties. **Figure 4** shows the absorption spectra for the different

View Article Online
DOI: 10.1039/D6MA00313C

Er_2O_3 concentration-doped glass samples. Nine absorption bands related to the ground state ($^4I_{15/2}$) to different excited states ($4G_{11/2}$, $4G(1)_{9/2}$, $4F_{3/2}$-$4F_{5/2}$, $4F_{7/2}$, $2H_{11/2}$, $4S_{3/2}$, $4F_{9/2}$, $4I_{9/2}$, and $4I_{11/2}$) transition can be seen, which correspond to 378, 407, 450, 488, 523, 543, 652, 794, and 977 nm. At 523 nm, there is also evidence of a hypersensitive transition ($^4I_{15/2}\rightarrow{}^2H_{11/2}$) following the selection rule $|\Delta S| = 0$, $|\Delta L| \leq 2$, $|\Delta J| \leq 2$. The absorption peaks' intensity showed gradual enhancement with the addition of Er_2O_3, which is in agreement with Mhareb et al.'s findings [46,47].

Mott and Davis suggested a relation to evaluating the energy band gap using the absorption data. **Figures 5 and 6** shows the Tauc plot, representing the relation between hv and $(\alpha hv)^2$. The synthesized glass system's optical properties are listed in Table 2. The Er1, Er2, Er3, and Er4 band gap (E_g) values are 3.553, 3.532, 3.521, and 3.516 eV, respectively. The gradual reduction can be noted by adding Er_2O_3 instead of B_2O_3, which relates to the formation of a novel valance–conduction bands localization due to defects. Conversely, **Table 2** assesses and lists the glass system's Urbach energy (E_U), where the E_U values can be seen to increase gradually by replacing B_2O_3 with Er_2O_3, and their values are 0.266, 0.268, 0.277, and 0.278 eV for Er1, Er2, Er3, and Er4. Such an increment is aligned with the band gap value reduction, indicating defects in glass samples. The glass samples' E_g–E_U relation is illustrated in **Figure 7**.

The glass samples' refractive index rises with increased Er_2O_3 content, referring to the increase of nonbridging oxygen (NBO) and polarizability. This argument is affirmed by electron polarizability with a 2.640 to 2.649 increase for Er1 and Er4. There was a 0.578 to 0.580 reflection loss value rise for Er1 and Er4, while the transmission reduced from 0.739 to 0.737 for Er1 and Er4. This trend can be related to the glass systems' increased refractive index. The metallization values lie between 0.421 and 0.419 for Er1 and Er4, which refers to the current

View Article Online
DOI: 10.1039/D6MA00313C

glasses' semiconductor behaviors. Lastly, there was an inverse optical electronegativity–optical basicity relation. Namely, a 0.955 to 0.945 optical electronegativity reduction for Er1 and Er4, where this reduction drove to lessen the glass system's link strength. Meanwhile, there was a 1.222 to 1.227 optical basicity increase for Er1 and Er4, representing ionic rather than covalent bond formation. This assumption indicates the glass's reduced stability, in line with forming NBO.

3.3. Mechanical and structural properties

The mechanical and structural properties can be used to evaluate glass stability. Theoretical models such as M-M are widely utilized for the calculation of the glasses' mechanical properties [36]. As the methodology part illustrated, the M-M model is reliant on dissociation energy (G_t) and packing density (V_t). Initially, we should analyze the rise in molar volume and density values described in **Tables 1** and **3**. This rise refers to reducing the glass compactness with increasing Er_2O_3 contents. This result aligns with packing density values, which were reduced by adding Er_2O_3, as shown in **Figure 8.** Besides, the dissociation energy for glass samples was reduced from 17.270 to 17.236 kcal/cm^3 for the Er1 and Er4 samples due to a weak bond (Er_2O_3) replacing a strong one (B_2O_3). For example, the dissociation energy for B_2O_3 and Er_2O_3 is 18.619 and 17.696 kcal/cm^3, respectively. Conversely, there was a 11.301 to 12.117 cm3/mol oxygen molar volume increase with rising Er_2O_3 content, owing to a large ionic radius atom (Er^{3+}) being added as opposed to a small one (B^{3+}), so the large ions disturb the glass networks by taking up greater space, resulting in an open glass structure, with this argument aligned with reducing glass compactness. This result is responsible for reducing the oxygen packing density from 88.485 to 82.527 mol/cm^3 for Er1 and Er4. There was a 0.281–0.267 Poisson ratio range for Er1 and Er4 samples. This result indicates that the glass samples have good density cross-linking. At the same

View Article Online
DOI: 10.1039/D6MA00313C

time, the fractal bond conductivity (d) values are in the 2.192–2.356 range, indicating that the glass network ranged from 2 to 3 dimensional. On the other hand, the hardness of the glass system was enhanced with rising Er_2O_3, referring to the glass samples' improved surface resistance against scratch tools. All elastic moduli showed a reduction by adding Er_2O_3, as **Figure 9** shows. For instance, the Shear modulus had a 38.126 to 36.228 GPa reduction for Er1 and Er4. The Young's modulus echoes this behavior and was reduced from 91.629 to 86.074 GPa for Er1 and Er4 samples. Such elastic moduli reduction is due to a weak bond (Er-O) replacing a strong one (B-O), as mentioned above. For an evaluation of the current sample's elastic modulus, we should compare it with other glass groups, for instance, comparative samples' Young's modulus values are (La2.5 = 90.235 GPa), (La5 = 87.15 GPa), (La7.5 = 84.484 GPa), (La10 = 82.153 GPa), (M1 = 91.657 GPa), (M2 = 90.043 GPa), (M3 = 88.538 GPa), (M4 = 87.130 GPa), (Nd2.5 = 89.993 GPa), (Nd5.0 = 86.697 GPa), (Nd7.5 = 83.858 GPa), (Pb1 = 90.620 GPa), (Pb2 = 87.296 GPa), (Pb3 = 84.030 GPa), and (Pb4 = 80.818 GPa), Y2.5 = 90.747 GPa), (Y5 = 87.887 GPa), and (Y7.5 = 85.244 GPa) [36,48–52]. The Er1 sample showed better results than the other samples, apart from M1.

3.4. Radiation shielding properties

As shown in **Figures 10(a-b)**, over the investigated γ-ray energy interval of 0.0332–2.506 MeV the LACs decreased exponentially under the influence of the interactions of photoelectric (PE) and Compton scattering (CS). The greatest LACs were found at 0.0332 MeV within the chosen energy interval. For Er1, Er2, Er3, and Er4 glass samples, the LACs respectively reach 44.725 cm^{-1}, 45.539 cm^{-1}, 46.731 cm^{-1}, and 48.144 cm^{-1}. With a gradual increase γ-ray energy in the 0.0332–0.122 MeV range, the LACs decreased by 95.39%, 94.78%, 94.22%, and 93.70% for the glass samples Er1, Er2, Er3, and Er4, in that order, under the PE interaction influence, as

View Article Online
DOI: 10.1039/D6MA00313C

illustrated in **Figure 10(a)**. This large reduction in LACs is explained by the decreasing interaction cross-section with γ-ray energy increase, whereby the cross-section fluctuates with $E_\gamma^{-3.5}$. Subsequently, with the advancement of CS interaction over the interval of 0.244–2.506 MeV, the prepared glass samples' LACs moderately fall. As shown in **Figure 10(b)**, the LACs decreased through 0.244–2.506 MeV throughout the following values: 0.624-0.144 cm^{-1} (Er1), 0.682-0.147 cm^{-1} (Er2), 0.740-0.150 cm^{-1} (Er3), and 0.798-0.154 cm^{-1} (Er1). The observed mild LAC decline in the prepared samples across the CS interval can be explained by the interaction cross-section's proportionality to E_γ^{-1}.

A comparison of the simulated LACs from MCNP and the XCOM database-calculated values is shown in **Table 4**, where the differences are up to ±1%, respectively. As illustrated in **Figure 11**, comparison was drawn between the prepared Er samples' LACs versus those of many commercial radiation shielding glasses as well as some comparable samples from literature in order to validate the prepared glass samples' shielding capacity. As clarified in **Figure 11**, at 0.662 MeV the Er1, Er2, Er3, and Er4 prepared glass samples' LACs are respectively 0.284, 0.293, 0.301, and 0.309 cm^{-1}, and are thus comparable to those of glass samples selected from literature [53–57] BaLi8, BaLi9, BaMo1, BaMo2, BaMo7, BaMo8, S1, S2, S5, X=15, Fe_2O_3, CuO, TiO_2, CaO, LiNb8, LiNb12 at 0.662 MeV with respective LACs of 0.278, 0.293, 0.280, 0.283, 0.301, 0.302, 0.279, 0.285, 0.300, 0.282, 0.312, 0.305, 0.299, 0.302, 0.278, 0.308, and 0.280 cm^{-1}. Moreover, the LACs of the fabricated Er1 glass samples were close to those for the commercial RS 323 G19 (0.280 cm^{-1}) radiation shielding glass which in its chemical composition has PbO of approximately 33 wt.%. Fabricated sample Er4 also has LAC at 0.662, close to that of the RS 360 commercial radiation shielding glass (0.320 cm^{-1}) which contains a high concentration of PbO reaches 45 wt.% [58] Moreover, the fabricated Er glass samples'

View Article Online
DOI: 10.1039/D6MA00313C

LACs are high in comparison to those reported for similar glasses selected from literature [53,56,57,59–66] for sample: BaLi1, BaLi2, BZLSn0, BZLSn5, BCrBi-0, BCrBi-25, ANBP00, ANBP10, SBC-B00, SBC-B10, SBC-B35, 0, 5, 20, X=5, BAlNaFe0, BAlNaFe3, LiNb0, LiNb2, MBTS0, BNLC0, BNLC2, BNLC10 with respective LACs of 0.175, 0.192, 0.226, 0.244, 0.185, 0.251, 0.161, 0.269, 0.222, 0.236, 0.267, 0.165, 0.167, 0.192, 0.202, 0.162, 0.166, 0.180, 0.210, 0.235, 0.162, 0.165, and 0.202 cm^{-1}. Also, the LACs of the current study's fabricated Er1-Er4 glasses are greater than those for the commercial RS253 (0.19 cm^{-1}) and RS253 G18 (0.19 cm^{-1}) radiation shielding glasses at 0.662 MeV [58]. In contrast, the LACs of Er1-Er4 are below those found in the literature [56,61,65,67,68] for glass sample ANBP20, ANBP50, X=50, X=55, MBTS35, MBTS70, A1, A4, LBWB0, LBWB1, LBWB4, and LBWB5 with LACs of 0.349, 0.501, 0.458, 0.478, 0.347, 0.423, 0.367, 0.433, 0.387, 0.380, 0.363, and 0.359 cm^{-1}, respectively.

Based on the fabricated Er glasses' measured ρ values and simulated LACs, the MACs were evaluated for Er1-Er4 glasses across the 0.0332–2.506 MeV interval, as **Figure 12 (a)** shows. The increase of γ-ray energy has an influence on the MACs similar that illustrated in **Figure 10** for the LACs, where the γ-ray energy rise exponentially reduces the MAC through the PE and CS interaction effect. As seen in **Figure 12 (a)**, the 0.0332–2.506 MeV increase declines the MACs throughout 11.927–0.038, 11.896–0.038, 11.967–0.039, and 12.090–0.039 cm^2/g for the Er1, Er2, Er3, and Er4 glass samples, respectively.

Figure 12 (b) illustrates the fabricated Er glass samples' inverse LAC–HVL relationship, as stated in **Eq. 9**. This relationship causes increased HVLs with greater γ-ray energy. With a 0.0332 to 2.506 MeV γ-ray energy increase, the HVLs for the developed Er1, Er2, Er3, and Er4 glass samples increased throughout 0.015–4.822, 0.015–4.712, 0.015–4.608, and 0.014–4.509 cm, respectively. The primary cause of the increase in HVLs is the fabricated Er glass samples'

View Article Online
DOI: 10.1039/D6MA00313C

decreased LACs; a decrease in the γ-photons' cross-section interaction is observed when the γ-ray energy is increased. As a result, while (I_t) photons increased, the interaction probability and (I_a) photons decreased. Therefore, the HVLs rise to approve the I_t=50% I_o relation.

Furthermore, as shown in Eq. 11, a (I_t) photon increase also increases the (I_t/I_o) ratios and TFs for the prepared Er glass samples. With a 0.122 and 2.506 MeV γ-ray energy increase, **Figure 12 (d)** reveals a TF increase over the 12.75–86.61 % (Er1), 9.27–86.32 % (Er2), 6.70–86.03 % (Er3), and 4.81–85.75 % (Er4) intervals. The data mentioned above verifies that photon absorption in the Er glass samples reaches its highest level during the PE interaction, whereas photon transmission falls to its minimum levels. As a result, the TFs are less than 1% in the $E_\gamma \leq$ 0.081 MeV energy interval. Subsequently, as the likelihood of PE reduced and the CS contacts grew, photon transmission exceeded photon absorption, resulting in a rise in the transmission ratio and TFs. **Figure 12 (d)** displays also high percentage of RPEs at low energy interval (PE interval), where the RPEs decrease throughout 100.00-87.25%, 100.00-90.73%, 100.00-93.30%, and 100.00-95.19%, respectively, for the Er1, Er2, Er3, and Er4 samples at 1 cm thickness. This is due to a 0.0332 to 0.122 MeV γ-ray energy increase. Because of the decrease in (I_a) photons, these high RPEs for prepared Er samples dramatically dropped with rising γ-photon energy over the CS interval. With a γ-ray energy increase to 2.506 MeV, the RPEs for a 1 cm thickness of the Er1, Er2, Er3, and Er4 glass samples decreased to 13.39%, 13.68%, 13.97%, and 14.25%, respectively, as illustrated in **Figure 12 (d)**.

Eq. 10, states that the Δ_{eq} is a comparison of photon transmission for prepared Er samples and pure lead element. The large reduction in the LACs for both lead and the prepared Er samples is responsible for the Δ_{eq} values' high reduction at low energy intervals, as seen in **Figure 12 (c)**. For instance, the LAC for Pb reduced by 85.54% with a γ-ray energy increase over the PE period

View Article Online
DOI: 10.1039/D6MA00313C

(i.e., $0.0332 < E_\gamma \leq 0.122$), but the LACs for the prepared glass samples Er1, Er2, Er3, and Er4 declined by 95.39%, 94.78%, 94.22%, and 93.70%, respectively. With a 0.0332 to 0.081 MeV γ-ray energy increase, the Δ_{eq} values decreased throughout 5.892–4.920, 5.787–4.143 cm, 5.639–3.613, and 5.474–3.212 cm for the Er1, Er2, Er3, and Er4 glass samples, respectively, due to the high declination of LACs for prepared glasses compared to that of pure lead. Because of the Pb's K-edges, the largest values of Δ_{eq} were seen at 0.122 MeV, where they reached 18.500, 16.023, 14.100, and 12.560 cm for glass samples Er1, Er2, Er3, and Er4, respectively. The reduction in LAC for lead (93.09%) during the CS interval is more than that seen in the investigated glass samples, whereas the decreases in LACs of the Er1, Er2, Er3, and Er4 glass samples are 76.98%, 78.44%, 79.68%, and 80.73%, respectively. The prepared Er glasses' moderate reduction in LACs results in a corresponding moderate reduction in Δ_{eq} values within the CS interval. The Δ_{eq} values were altered throughout the ranges of 11.422–3.427, 10.453–3.349, 9.633–3.275, and 8.938–3.205 cm for the ER1, Er2, Er3, and Er4 glass samples, respectively, due to the γ-ray energy increase within the 0.244–2.506 MeV interval.

As seen in **Figure 13 (a-d)**, the produced samples' radiation shielding properties are impacted by an increase in Er_2O_3 concentrations, contingent upon the Er glass samples' chemical composition. The manufactured Er glass samples' density increases with increasing Er_2O_3 concentration between 1.25 and 5 mol%, reaching 3.750 and 3.982 g/cm^3, respectively. When the manufactured glass samples' Er_2O_3 concentration replaced those of B_2O_3, the electron density and effective atomic number (Z_{eff}) increased [69,70]. This led to a rise in sample density. The efficiency of prepared glasses' radiation shielding was investigated at PE and SC intervals, as previously demonstrated. For both PE and CS interactions, the photon cross-section of interaction is proportional to $Z_{eff}^{4.6}$ and Z_{eff}, respectively, over these two intervals. Therefore, the

View Article Online
DOI: 10.1039/D6MA00313C

rise in the Z_{eff} greatly boosts the radiation shielding properties in the PE interval, although a minor enhance was found across the CS interval. When the Er_2O_3 concentrations rose between 1.25 and 5 mol.%, **Figure 13 (a)** indicates an enhancement in the LACs by 54.94%, 8.78%, and 5.93%, respectively, at 0.059, 0.662, and 1.408 MeV. For prepared glass samples, there is a decrease in the necessary HVLs and (I_t) photons after a LAC increase. As **Figure 13 (b)** illustrates, a Er_2O_3 concentration increase between 1.25 and 5.00 mol% reduces the HVLs at 0.059, 0.662, and 2.506 MeV in the 0.058–0.037, 2.439–2.243, and 4.822–4.509 cm ranges, respectively. There is (I_a) photon growth along with the aforementioned (I_t) photon reduction. Consequently, as the Er_2O_3 level was raised, the RPEs of the produced glass samples increased in certain intervals, as **Figure 13 (d)** shows at 24.74–26.59% (0.662 MeV) and 13.39–14.25% (2.506 MeV) as the Er_2O_3 level increases from 1.25 to 5.00 mol%. At 0.059 MeV, the RPEs of every sample are almost 100%. Furthermore, the manufactured Er glass samples' Δ_{eq} is decreased by the rise in μ values brought on by the increased Er_2O_3 content. **Figure 13 (c)** shows the Δ_{eq} values to drop over 4.928–3.181 cm (0.059 MeV), 4.386–4.032 cm (0.662 MeV), and 3.427–3.205 cm (2.506 MeV) with an increase in the Er_2O_3 concentration between 1.25-5.00 mol%.

As shown in **Figure 14 (a) and (b)**, the produced samples Er1, Er2, Er3, and Er4 have RPEs that grow with a 0.25 to 2 cm thickness increase, decreasing the TFs dramatically. Within the samples, the γ-photon–electron interaction probability increases with increased sample thickness. For every sample under investigation, this rise in the interaction probability results in a (I_a/I_o) ratio increase and a (I_t/I_o) ratio decrease. As seen in **Figure 14 (a)**, this decline in the (I_t/I_o) ratios caused a drop in the TFs for every sample that was examined. The Er1, Er2, Er3, and Er4 prepared samples' TF values decrease with a 0.25 to 2 cm glass thickness increase at 93.14–56.65%, 92.95–55.70%, 92.75–54.78%, and 92.56–53.89%, respectively. As demonstrated in

View Article Online
DOI: 10.1039/D6MA00313C

Figure 14 (b), in contrast, with a 0.25 to 2 cm glass thickness increase, the RPEs increased over the interval of 6.857–43.352%, 7.055–44.305%, 7.247–45.219%, and 7.436–46.108%, respectively, for prepared glass samples Er1, Er2, Er3, and Er4.

4. Conclusion:

In summary,

- A group of four transparent pink bulk glasses were successfully fabricated via melting and later annealing with composition formula of $(TeO_2)_{20}(GeO_2)_{10}(B_2O_3)_{35-x}(MgO)_{35}(Er_2O_3)_x$ with x values of 1.25, 2.5, 3.75, and 5 which represents the erbium oxide concentration.
- The XRD profile provides confirmation of the glass's random structure, confirming the amorphous structure with a broad band at 28 and 50 degrees.
- The absorption spectra for glass samples doped with different Er_2O_3 concentrations shows nine absorption bands related to the ground state ($^4I_{15/2}$) to different excited states ($4G_{11/2}$, $4G(1)_{9/2}$, $4F_{3/2}$-$4F_{5/2}$, $4F_{7/2}$, $2H_{11/2}$, $4S_{3/2}$, $4F_{9/2}$, $4I_{9/2}$, and $4I_{11/2}$) transition, which correspond to 378, 407, 450, 488, 523, 543, 652, 794, and 977 nm.
- The adding of Er_2O_3 to glass system reduced the band gap (E_g) values which ranged from 3.553, to 3.516 eV, respectively. E_U values increased gradually by replacing B_2O_3 with Er_2O_3, and their values are 0.266, 0.268, 0.277, and 0.278 eV for Er1, Er2, Er3, and Er4.
- The dissociation energy for glass samples was reduced from 17.270 to 17.236 kcal/cm^3 for Er1 and Er4 samples due to a strong bond (B_2O_3) being replaced with a weak one (Er_2O_3). This result led to reduce the elastic moduli by adding Er_2O_3 to glass system.

View Article Online
DOI: 10.1039/D6MA00313C

- Regarding the γ-ray protection capacity, it is increased with the prepared boro-tellurite glasses' increased Er_2O_3 content. The enrichment in the Er_2O_3 concentration in the range of 1.25–5 mol% raises the prepared samples' LAC within ranges of 0.624–0.798 cm^{-1} (0.244 MeV), 0.331–0.368 cm^{-1} (0.662 MeV), 0.206–0.219 cm^{-1} (1.173 MeV), and 0.144–0.154 cm^{-1} (2.506 MeV). The LAC increase reduces the required half-value thickness by 35.46%, 21.75%, 9.98%, and 6.49% respectively at 0.059, 0.244, 0.511, and 2.506 MeV. Furthermore, Er_2O_3 addition up to 5 mol% increases the RPE for 1 cm thickness of prepared samples to 26.6% at 0.662 MeV. After that, the aforementioned RPE further increased to 46.10% when the prepared glass thickness was raised to 2 cm.
- The main finding of the manuscript is that Er2O3 addition to Germanium boro-tellurite glasses slightly reduced the prepared glasses' optical and mechanical properties. On the other hand, radiation protective properties were enhanced, making them a good lead-free alternative material for radiation protective applications.

Acknowledgments: The authors acknowledge the financial support from the Manipal Academy of Higher Education, Manipal, India.

Compliance with Ethical Standards: Authors declare that this manuscript is original, has not been published before, and is not currently being considered for publication elsewhere.

Data Availability Statements: The raw/processed data required to reproduce the above findings are available on request.

Supplementary information: Not Applicable

Ethical approval: Not Applicable

Conflict of interest: The authors declare that they have no conflict of interest.

Funding Declaration: The authors acknowledge the financial support from the Manipal Academy of Higher Education, Manipal, India.

View Article Online
DOI: 10.1039/D6MA00313C

Authors Contributions: KAM, MIS, KAM, MHAM, IAJ, SDK: Conceptualization, Methodology, Software, Validation, Investigation, Data Curation, Writing-Review and Editing, Visualization, Supervision

References

1 A. M. Alsharari, A. Alatawi, S. A. M. Issa, M. Rashad, A. A. A. Darwish, Y. B. Saddeek Radiation protection parameters of glasses with different yttria additives at different photon energies. (2019) *Mater. Res. Express*. **6**, 125201.

2 D. A. Aloraini, A. H. Almuqrin, K. M. Kaky, M. I. Sayyed, M. Elsafi Radiation shielding capability and exposure buildup factor of cerium(iv) oxide-reinforced polyester resins. (2023) *E-Polymers*. **23**,.

3 M. I. Sayyed, K. M. Kaky, M. H. A. Mhareb, A. Al-keisy, S. O. Baki Impact of CuO on TeO2–GeO2–ZnO–Al2O3–MgO glass system for ionizing shielding applications. (2023) *Journal of Materials Science: Materials in Electronics*. **34**, 2277.

4 S. A. M. Issa, A. M. Hassan, M. Algethami, H. M. H. Zakaly Structural, linear/nonlinear optical characteristics and radiation shielding effectiveness of Cu4O3/Cu2O dual-phase thin films: Influence of oxygen flow rate in reactive sputtering process. (2024) *Ceram. Int.* **50**, 38281–38292.

5 K. V. Rao, M. Madhu, P. Ashok, G. A. Kumar, R. K. Guntu Radiation Shielding, EPR, and TL Mechanism in Cr3+: Ba(La)2SiO6 Glass Ceramics. (2022) *Silicon*. **14**, 9887–9899.

6 A. Saleh, M. G. El-Feky, M. S. Hafiz, N. A. Kawady Experimental and theoretical investigation on physical, structure and protection features of TeO2–B2O3 glass doped with PbO in terms of gamma, neutron, proton and alpha particles. (2023) *Radiation Physics and Chemistry*. **202**, 110586.

7 I. G. Geidam, K. A. Matori, M. K. Halimah, K. T. Chan, F. D. Muhammad, M. Ishak, et al. Oxide ion polarizabilities and gamma radiation shielding features of TeO2–B2O3–SiO2 glasses containing Bi2O3 using Phy-X/PSD software. (2022) *Mater. Today Commun.* **31**, 103472.

8 B. Aktas, A. Acikgoz, D. Yilmaz, S. Yalcin, K. Dogru, N. Yorulmaz The role of TeO2 insertion on the radiation shielding, structural and physical properties of borosilicate glasses. (2022) *Journal of Nuclear Materials*. **563**, 153619.

9 A. L. Kozlovskiy, M. V. Zdorovets Effect of doping of Ce4+/3+ on optical, strength and shielding properties of (0.5-x)TeO2-0.25MoO-0.25Bi2O3-xCeO2 glasses. (2021) *Mater. Chem. Phys.* **263**, 124444.

View Article Online
DOI: 10.1039/D6MA00313C

10 M. I. Sayyed, M. H. A. Mhareb, B. C. Şakar, K. A. Mahmoud, E. Şakar, H. A. Thabit, et al. Experimental investigation of structural and radiation shielding features of Li2O-BaO-ZnO-B2O3-Bi2O3 glass systems. (2024) *Radiation Physics and Chemistry*. **218**, 111640.

11 B. B. Solak, B. Aktas, D. Yilmaz, S. Kalecik, S. Yalcin, A. Acikgoz, et al. Exploring the radiation shielding properties of B2O3-PbO-TeO2-CeO2-WO3 glasses: A comprehensive study on structural, mechanical, gamma, and neutron attenuation characteristics. (2024) *Mater. Chem. Phys.* **312**, 128672.

12 M. Fidan, A. Acikgoz, G. Demircan, D. Yilmaz, B. Aktas Optical, structural, physical, and nuclear shielding properties, and albedo parameters of TeO2–BaO–B2O3–PbO–V2O5 glasses. (2022) *Journal of Physics and Chemistry of Solids*. **163**, 110543.

13 S. A. M. Issa, M. Rashad, T. A. Hanafy, Y. B. Saddeek Experimental investigations on elastic and radiation shielding parameters of WO3-B2O3-TeO2 glasses. (2020) *J. Non. Cryst. Solids*. **544**, 120207.

14 M. I. Sayyed, M. H. A. Mhareb, K. M. Kaky Characterization of Mechanical and Radiation Shielding Features of Borosilicate Glasses Doped with MoO3. (2024) *Silicon*. **16**, 1955–1965.

15 K. M. Kaky, M. I. Sayyed The Radiation Shielding Parameters of a Standard Silica Glass System. (2024) *Silicon*. **16**, 1197–1203.

16 R. Boodaghi Malidarre, I. Akkurt, O. Kocar, I. Ekmekci Analysis of radiation shielding, physical and optical qualities of various rare earth dopants on barium tellurite glasses: A comparative study. (2023) *Radiation Physics and Chemistry*. **207**, 110823.

17 S. Yasmin, M. Saifuddin, S. Chakraborty, A. Meaze, B. Barua Evaluation of TeO2-WO3-Bi2O3 glasses for their potential in radiation shielding with the utilization of the Phy-X software program. (2024) *Nexus of Future Materials*. **1**, 51–55.

18 H. M. H. Zakaly, S. A. M. Issa, H. A. Saudi, T. S. Soliman Decoding the role of bismuth oxide in advancing structural, thermal, and nuclear properties of [B2O3–Li2O–SiO2]-Nb2O5 glass systems. (2024) *Radiation Physics and Chemistry*. **223**, 111984.

19 N. Effendy, M. H. M. Zaid, K. A. Matori, S. M. Iskandar, R. Hisam, M. N. Azlan, et al. Fabrication of novel BaO–Al2O3–Bi2O3–B2O3 glass system: Comprehensive study on elastic, mechanical and shielding properties. (2022) *Progress in Nuclear Energy*. **153**, 104418.

20 M. I. Sayyed, B. Albarzan, A. H. Almuqrin, A. M. El-Khatib, A. Kumar, D. I. Tishkevich, et al. Experimental and Theoretical Study of Radiation Shielding Features of CaO-K2O-Na2O-P2O5 Glass Systems. (2021) *Materials*. **14**, 3772.

21 M. S. Al-Buriahi, M. I. Sayyed, Y. Al-Hadeethi Role of TeO2 in radiation shielding characteristics of calcium boro-tellurite glasses. (2020) *Ceram. Int.* **46**, 13622–13629.

22 S. Bilici, M. Kamislioglu, E. E. Altunsoy Guclu A Monte Carlo simulation study on the evaluation of radiation protection properties of spectacle lens materials. (2023) *The European Physical Journal Plus*. **138**, 80.

View Article Online
DOI: 10.1039/D6MA00313C

23 M. Kamislioglu Research on the effects of bismuth borate glass system on nuclear radiation shielding parameters. (2021) *Results Phys.* **22**, 103844.

24 M. I. Sayyed, K. A. Mahmoud, F. Q. Mohammed, K. M. Kaky A comprehensive evaluation of Mg-Ni based alloys radiation shielding features for nuclear protection applications. (2023) *Nuclear Engineering and Technology*.

25 G. Kilic, E. Ilik, S. A. M. Issa, B. Issa, M. S. Al-Buriahi, U. G. Issever, et al. Ytterbium (III) oxide reinforced novel TeO2–B2O3–V2O5 glass system: Synthesis and optical, structural, physical and thermal properties. (2021) *Ceram. Int.* **47**, 18517–18531.

26 G. Kilic, E. Ilik, S. A. M. Issa, H. O. Tekin Synthesis and structural, optical, physical properties of Gadolinium (III) oxide reinforced TeO2–B2O3–(20-x)Li2O-xGd2O3 glass system. (2021) *J. Alloys Compd.* **877**, 160302.

27 S. Yasmin, M. Kamislioglu, M. I. Sayyed Assessment of radiation shielding performance of Li2O-BaO-Bi2O3-P2O5 glass systems within the energy range from 0.081 MeV to 1.332 MeV via MCNP6 code. (2023) *Optik (Stuttg).* **274**, 170529.

28 M. Kamislioglu An investigation into gamma radiation shielding parameters of the (Al:Si) and (Al+Na):Si-doped international simple glasses (ISG) used in nuclear waste management, deploying Phy-X/PSD and SRIM software. (2021) *Journal of Materials Science: Materials in Electronics*. **32**, 12690–12704.

29 L. Gerward, N. Guilbert, K. Bjørn Jensen, H. Levring X-ray absorption in matter. Reengineering XCOM. (2001) *Radiation Physics and Chemistry*. **60**, 23–24.

30 E. Şakar, Ö. F. Özpolat, B. Alım, M. I. Sayyed, M. Kurudirek Phy-X / PSD: Development of a user friendly online software for calculation of parameters relevant to radiation shielding and dosimetry. (2020) *Radiation Physics and Chemistry*. **166**,.

31 E. O. Ulas, A. Acikgoz, B. Aktas, Y. Kavun Influence of B2O3 incorporation on the structural, mechanical and radiation shielding properties of TeO2 Based bioglasses. (2025) *Applied Radiation and Isotopes*. **221**, 111799.

32 M. Fidan, A. Acikgoz, D. Yılmaz, G. Demircan, S. Kalecik, B. Aktas, et al. Investigation of the structural, mechanical, radiation and neutron shielding properties of the TeO2-B2O3-Li2O-MoO3-CuO glass system. (2024) *J. Alloys Compd.* **976**, 172981.

33 N. F. Mott, E. A. Davies (1979) Electronic Processes in Non-Crystalline Materials. Clarendon Press, Oxford, .

34 O. B. Aljewaw, M. K. A. Karim, H. M. Kamari, M. H. M. Zaid, A. A. Salim, M. H. A. Mhareb Physical and spectroscopic characteristics of lithium-aluminium-borate glass: Effects of varying Nd2O3 doping contents. (2022) *J. Non. Cryst. Solids*. **575**, 121214.

35 M. H. A. Mhareb, M. A. Morsy, H. Almarri, M. I. Sayyed, I. Alrammah, N. Alonizan, et al. Gamma-ray induced effect on the structural and optical properties and durability of neodymium-doped zinc–bismuth–borotellurite glasses and glass ceramics. (2023) *Opt. Mater. (Amst).* **137**, 113572.

View Article Online
DOI: 10.1039/D6MA00313C

36 A. Makishima, J. D. Mackenzie Calculation of bulk modulus, shear modulus and Poisson's ratio of glass. (1975) *J. Non. Cryst. Solids*. **17**, 147–157.

37 N. R. K. Chand, B. K. Sudhakar, G. Ravikumar, G. S. Rao, C. S. Rao Influence of manganese ions on elastic and spectroscopic properties of ZnO doped novel calcium fluorophosphate bio active glasses. (2021) *Phys. Scr.* **96**, 125020.

38 M. H. A. Mhareb, Y. S. M. Alajerami, M. I. Sayyed, K. A. Mahmoud, T. Ghrib, M. K. Hamad, et al. Morphological, optical, structural, mechanical, and radiation-shielding properties of borosilicate glass–ceramic system. (2022) *Ceram. Int.* **48**,.

39 B. Aktas, S. Yalcin, M. Albaskara, E. Aytar, G. Ceyhan, Z. Ş. Turhan Effect of Er2O3 on structural, mechanical, and optical properties of Al2O3-Na2O-B2O3-SiO2 glass. (2022) *J. Non. Cryst. Solids*. **584**, 121516.

40 X-5 Monte Carlo Team MCNP — A General Monte Carlo N-Particle Transport Code, Version 5. (2003) *La-Ur-03-1987*. **II**,.

41 K. G. Mahmoud, O. L. Tashlykov, S. Praveenkumar, M. I. Sayyed, S. Hashim Synthesis of a new epoxy resin reinforced by ZnO nanoparticles for γ-ray shielding purposes: Experimental and Monte Carlo simulation assesments. (2023) *Radiation Physics and Chemistry*. **208**, 110938.

42 I. G. Alhindawy, H. Gamal, A. H. Almuqrin, M. I. Sayyed, K. A. Mahmoud Impacts of the calcination temperature on the structural and radiation shielding properties of the NASICON compound synthesized from zircon minerals. (2023) *Nuclear Engineering and Technology*. **55**,.

43 R. K. Guntu EPR-TL correlation, in radiation shielding Ba(10-x)MnxLa30Si60 glasses. (2022) *J. Mol. Struct.* **1248**, 131533.

44 S. Y. Rasul, B. Aktas, D. Yilmaz, A. F. Pathman, S. Yalcin, A. Acikgoz Impact of HfO2 on the structural, thermal, gamma, and neutron shielding properties of boro-tellurite glasses. (2025) *Inorg. Chem. Commun.* **174**, 113993.

45 K. Dogru, B. Aktas, A. Acikgoz, D. Yilmaz, A. F. Pathman, S. Yalcin, et al. Structural, thermal, and radiation shielding properties of B2O3-TeO2-Bi2O3-CdO-Tm2O3 glasses: The role of Tm2O3. (2024) *Ceram. Int.* **50**, 47384–47394.

46 S. N. Nazrin, M. K. Halimah, F. D. Muhammad Comparison study of optical properties on erbium-doped and silver-doped zinc tellurite glass system for non-linear application. (2019) *Journal of Materials Science: Materials in Electronics*. **30**, 6378–6389.

47 M. H. A. Mhareb Physical, optical and shielding features of Li2O–B2O3–MgO–Er2O3 glasses co-doped of Sm2O3. (2020) *Appl. Phys. A Mater. Sci. Process.* **126**,.

48 M. I. Sayyed, M. J. Zaiter, M. H. A. Mhareb, K. A. Mahmoud, S. Biradar, R. I. Mahdi, et al. Optical, physical, mechanical, structural, and radiation shielding investigations of B2O3–TeO2-GeO2-MgO-PbO for ionizing protection and optical transmission application. (2024) *Opt. Mater. (Amst).* **154**, 115807.

View Article Online
DOI: 10.1039/D6MA00313C

49 M. I. Sayyed, M. H. A. Mhareb, M. K. Hamad, A. J. Kadhim, H. M. Alsafi, K. A. Mahmoud, et al. Effects of MoO3 on the structural, physical, mechanical, optical, and ionizing shielding of borate-germanate-telluride glass system. (2024) *Ceram. Int.* **50**, 46008–46017.

50 M. H. A. Mhareb, M. I. Sayyed, R. I. Mahdi, K. M. Kaky, M. K. Hamad, A. J. Kadhim Role of Nd (III) ions on B2O3–TeO2-GeO2-MgO glass composition for optical and ionizing protection application. (2024) *Nuclear Engineering and Technology*. 103162.

51 K. M. Kaky, M. I. Sayyed, K. A. Mahmoud, M. H. A. Mhareb, S. Biradar, A. J. Kadhim A comprehensive investigation on lanthanum ions doped borate-tellurite-germinate glass for radiation shielding and optical application. (2024) *Progress in Nuclear Energy*. **176**, 105402.

52 M. I. Sayyed, M. H. A. Mhareb, R. I. Mahdi, A. J. Kadhim, K. M. Kaky, M. K. Hamad Design, fabrication, and features investigations of high concentration of Yttrium Oxide doped germanate tellurate borate glass system for optical and radiation shielding application. (2024) *Ceram. Int.* **50**, 54490–54497.

53 Y. Al-Hadeethi, M. I. Sayyed BaO–Li2O–B2O3 glass systems: Potential utilization in gamma radiation protection. (2020) *Progress in Nuclear Energy*. **129**, 103511.

54 O. Agar, M. I. Sayyed, H. O. Tekin, K. M. Kaky, S. O. Baki, I. Kityk An investigation on shielding properties of BaO, MoO3 and P2O5 based glasses using MCNPX code. (2019) *Results Phys.* **12**, 629–634.

55 G. ALMisned, W. Elshami, S. Issa, G. Susoy, H. Zakaly, M. Algethami, et al. Enhancement of Gamma-ray Shielding Properties in Cobalt-Doped Heavy Metal Borate Glasses: The Role of Lanthanum Oxide Reinforcement. (2021) *Materials*. **14**, 7703.

56 P. Limkitjaroenporn, J. Kaewkhao, P. Limsuwan, W. Chewpraditkul Physical, optical, structural and gamma-ray shielding properties of lead sodium borate glasses. (2011) *Journal of Physics and Chemistry of Solids*. **72**, 245–251.

57 K. S. Shaaban, T. M. Althagafi, A. Ashour, A. Alalawi, M. S. Al-Buriahi, A. A. Ibraheem The role of Nb2O5 on structural, mechanical, and gamma-ray shielding characteristics of lithium molybdenum borate glasses. (2024) *Radiation Physics and Chemistry*. **216**, 111440.

58 Schott AG (2013) Radiation Shielding Glasses. Hattenbergstrasse 10 55122 Mainz Germany.

59 M. I. Sayyed, A. H. Almuqrin, K. A. Mahmoud, A. S. Abouhaswa Influence of increasing SnO2 content on the mechanical, optical, and gamma-ray shielding characteristics of a lithium zinc borate glass system. (2022) *Sci. Rep.* **12**, 1800.

60 Y. Al-Hadeethi, M. I. Sayyed, A. Z. Barasheed, M. Ahmed, M. Elsafi Fabrication of Lead Free Borate Glasses Modified by Bismuth Oxide for Gamma Ray Protection Applications. (2022) *Materials*. **15**, 789.

61 M. S. Al-Buriahi, Y. S. Rammah Investigation of the physical properties and gamma-ray shielding capability of borate glasses containing PbO, Al2O3 and Na2O. (2019) *Applied Physics A*. **125**, 717.

View Article Online
DOI: 10.1039/D6MA00313C

62 M. S. Al-Buriahi, C. Sriwunkum, H. Arslan, B. T. Tonguc, M. A. Bourham Investigation of barium borate glasses for radiation shielding applications. (2020) *Applied Physics A*. **126**, 68.

63 A. Saber, A.- Moety, W. A. El-Gammal, S. M. Salem, A. S. Mahmoud, M. M. H. Eshtewi, et al. Gamma-Ray Shielding Parameters of Some Sodium-Borate Glasses Containing BaO and As2 O3. (2017) *International Journal of Scientific Research in Science, Engineering and Technology (IJSRSET)*. **3**, 1144–1150.

64 M. S. Sadeq, O. I. Sallam, E. M. Sedqy Shielding parameters and optical stability of sodium alumino-borate glasses against gamma rays by iron oxide additives. (2024) *Opt. Mater. (Amst).* **150**, 115234.

65 A. Alshamari, M. H. A. Mhareb, N. Alonizan, N. Dwaikat, I. Alrammah, M. Alsuhybani, et al. Influence of various gamma-ray doses on radiation shielding, thermal, mechanical, structural, and optical properties of tellurite, borate, and boro-tellurite glasses modified with molybdenum and strontium oxide. (2023) *Opt. Mater. (Amst).* **142**, 114159.

66 K. A. Mahmoud, F. I. El-Agwany, Y. S. Rammah, O. L. Tashlykov Gamma ray shielding capacity and build up factors of CdO doped lithium borate glasses: theoretical and simulation study. (2020) *J. Non. Cryst. Solids*. **541**,.

67 D. A. Aloraini, M. I. Sayyed, J. F. M. Jecong, A. Kumar, B. O. Elbashir, A. A. H. Almuqrin, et al. Structural and gamma ray shielding behavior of dual heavy metal oxide doped magnesium sodium borate glasses. (2022) *Optik (Stuttg).* **268**, 169771.

68 S. Stalin, D. K. Gaikwad, M. S. Al-Buriahi, C. Srinivasu, S. A. Ahmed, H. O. Tekin, et al. Influence of Bi2O3/WO3 substitution on the optical, mechanical, chemical durability and gamma ray shielding properties of lithium-borate glasses. (2021) *Ceram. Int.* **47**, 5286–5299.

69 D. Yılmaz, B. Aktaş, Ş. Yalçın, M. Albaşkara Erbium oxide and Cerium oxide-doped borosilicate glasses as radiation shielding material. (2020) *Radiation Effects and Defects in Solids*. **175**, 458–471.

70 S. Yalcin, B. Aktas, D. Yilmaz Radiation shielding properties of Cerium oxide and Erbium oxide doped obsidian glass. (2019) *Radiation Physics and Chemistry*. **160**, 83–88.

View Article Online
DOI: 10.1039/D6MA00313C

Table 1: Chemical formula of Erbium Doped G-T-B Glass System

Glass code	Chemical composition (mol%)					Density (g/cm^3)
	B_2O_3	TeO_2	GeO_2	MgO	Er_2O_3	
Er1	33.75	20.00	10.00	35.00	1.25	3.750±0.059
Er2	32.50	20.00	10.00	35.00	2.50	3.828±0.056
Er3	31.25	20.00	10.00	35.00	3.75	3.905±0.066
Er4	30.00	20.00	10.00	35.00	5.00	3.982±0.072

Table 2: Er_2O_3-doped glass samples' optical parameters

Optical parameters	Glass codes			
	Er1	Er2	Er3	Er4
Indirect band gap (eV)	3.553±0.02	3.532±0.02	3.521±0.02	3.516±0.02
Direct band gap (eV)	3.437±0.02	3.417±0.02	3.394±0.02	3.371±0.02
Refractive index	2.262	2.266	2.269	2.270
Transmission	0.739	0.738	0.738	0.737
Urbach energy (eV)	0.266	0.268	0.277	0.278
Reflection loss (R)	0.578	0.579	0.580	0.580
Metallization	0.421	0.420	0.419	0.419
Optical electronegativity (χ)	0.955	0.949	0.946	0.945
Electron polarizability (α_o)	2.640	2.645	2.648	2.649
Optical basicity (Λ)	1.222	1.225	1.226	1.227

Table 3: Mechanical parameters for glass samples doped with Er_2O_3

Mechanical parameters	Glass codes			
	Er1	Er2	Er3	Er4
Molar volume (V_m, cm^3/mol)	22.602	23.168	23.711	24.234
Oxygen Molar Volume (OMV, cm^3/mol)	11.301	11.584	11.855	12.117
Oxygen Packing Density (OPD, mol/cm^3)	88.485	86.324	84.345	82.527
Packing factor (V_i)	14.344	14.388	14.432	14.476
Packing density (V_t)	0.634	0.621	0.608	0.597
Poisson ratio (σ)	0.281	0.276	0.271	0.267
Hardness (H, GPa)	5.217	5.233	5.248	5.263
Dissociation energy (G_t, kcal/cm^3)	17.270	17.259	17.247	17.236
Young's modulus (Y, GPa)	91.629±1.441	89.605±1.310	87.761±1.483	86.074±1.556
Bulk modulus (GPa)	69.556	66.563	63.893	61.501
Shear modulus (GPa)	38.126	37.434	36.804	36.228
Longitudinal modulus (GPa)	120.392	116.475	112.966	109.806
Fractal bond conductivity (d)	2.192	2.249	2.304	2.356

View Article Online
DOI: 10.1039/D6MA00313C

Table 4. Comparing the linear attenuation coefficient obtained from the simulation code MCNP-5 and those calculated using the XCOM database

Energy (MeV)	Linear attenuation coefficient (cm^{-1})											
	E1			E2			E3			E4		
	MCNP ±0.1	XCOM ±1	Diff (%)	MCNP ±0.1	XCOM ±1	Diff (%)	MCNP ±0.1	XCOM ±1	Diff (%)	MCNP ±0.1	XCOM ±1	Diff (%)
0.0332	44.725	44.325	-0.9	45.539	45.706	0.4	46.731	47.055	0.7	48.144	48.381	0.5
0.059	12.038	12.041	0.0	14.297	14.313	0.1	16.369	16.483	0.7	18.651	18.576	-0.4
0.081	5.397	5.366	-0.6	6.410	6.366	-0.7	7.351	7.326	-0.3	8.268	8.247	-0.3
0.122	2.060	2.042	-0.9	2.378	2.383	0.2	2.702	2.709	0.2	3.034	3.024	-0.3
0.244	0.624	0.625	0.1	0.682	0.683	0.2	0.740	0.739	-0.1	0.798	0.793	-0.6
0.356	0.428	0.429	0.2	0.453	0.454	0.3	0.477	0.478	0.3	0.500	0.501	0.3
0.511	0.331	0.332	0.2	0.344	0.345	0.2	0.356	0.357	0.2	0.368	0.369	0.2
0.662	0.284	0.285	0.2	0.293	0.293	0.2	0.301	0.302	0.2	0.309	0.310	0.2
1.173	0.206	0.208	1.0	0.210	0.213	1.1	0.215	0.217	1.1	0.219	0.221	1.2
1.332	0.193	0.195	0.8	0.197	0.199	0.9	0.201	0.203	1.0	0.205	0.207	1.0
1.408	0.188	0.189	0.8	0.191	0.193	0.9	0.195	0.197	0.9	0.199	0.201	1.0
2.506	0.144	0.144	0.4	0.147	0.148	0.4	0.150	0.151	0.5	0.154	0.154	0.5

View Article Online
DOI: 10.1039/D6MA00313C

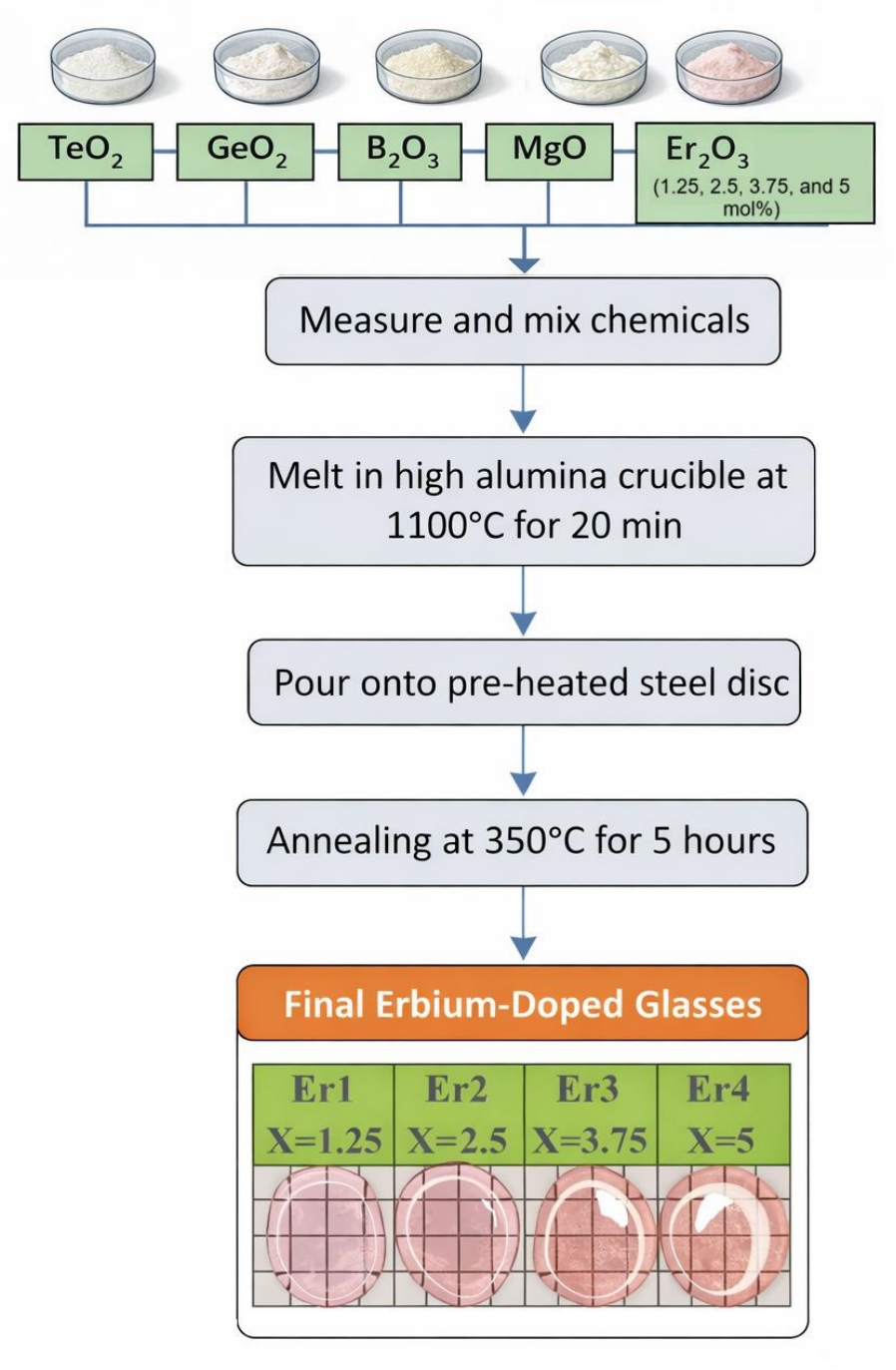

Figure 1: A photograph of erbium doped G-T-B glass system

View Article Online
DOI: 10.1039/D6MA00313C

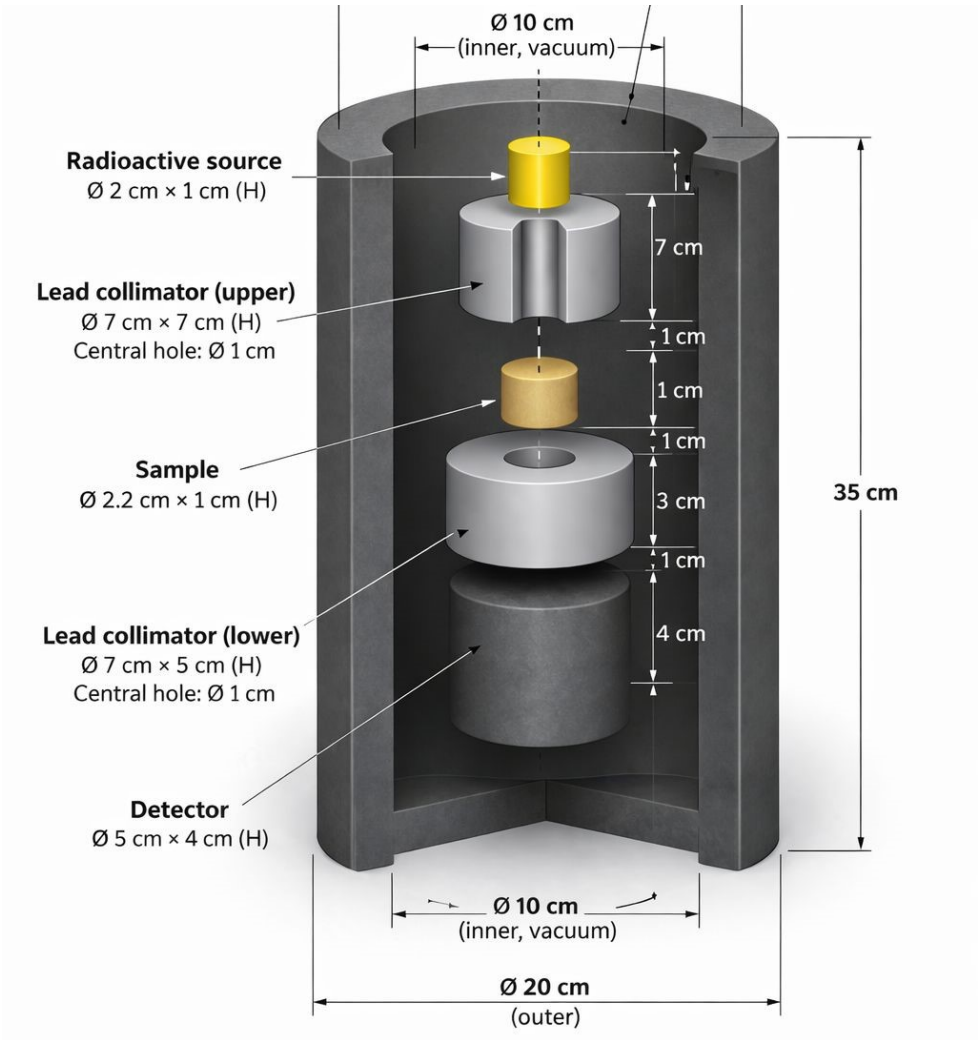

Figure 2: A 3D representation for the geometry according to the MCNP-5's input file

View Article Online
DOI: 10.1039/D6MA00313C

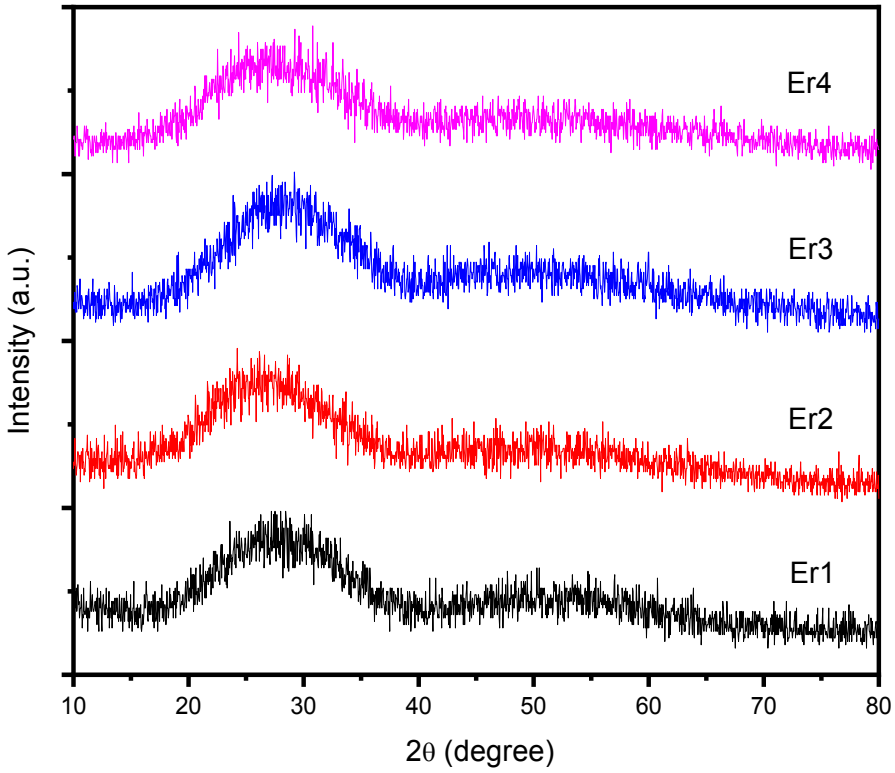

Figure 3: XRD results for all glass samples.

View Article Online
DOI: 10.1039/D6MA00313C

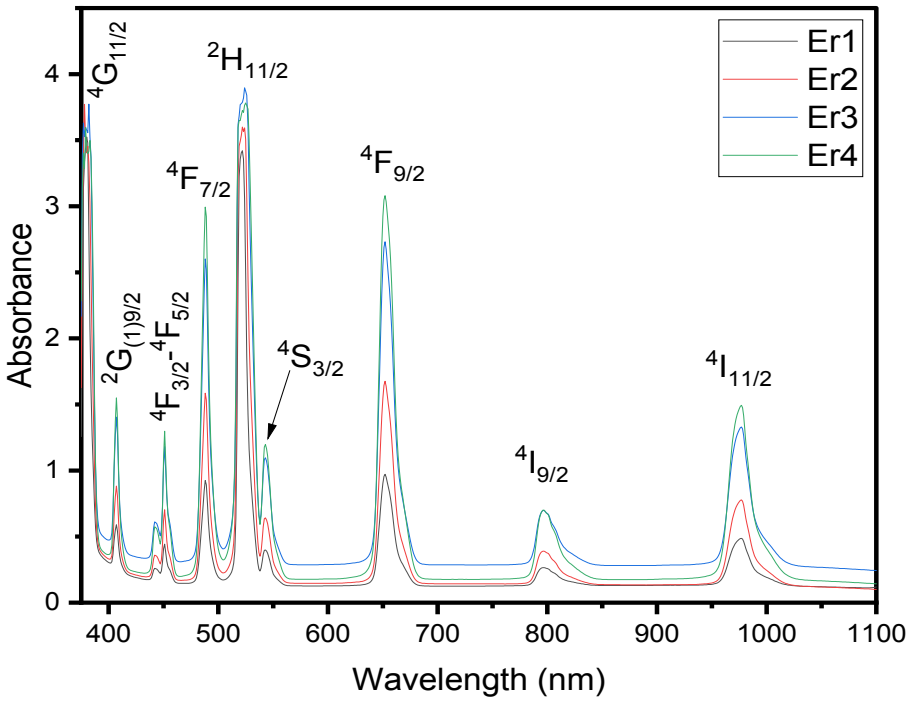

Figure 4: UV-vis absorption spectra for Er_2O_3-doped glass samples.

View Article Online
DOI: 10.1039/D6MA00313C

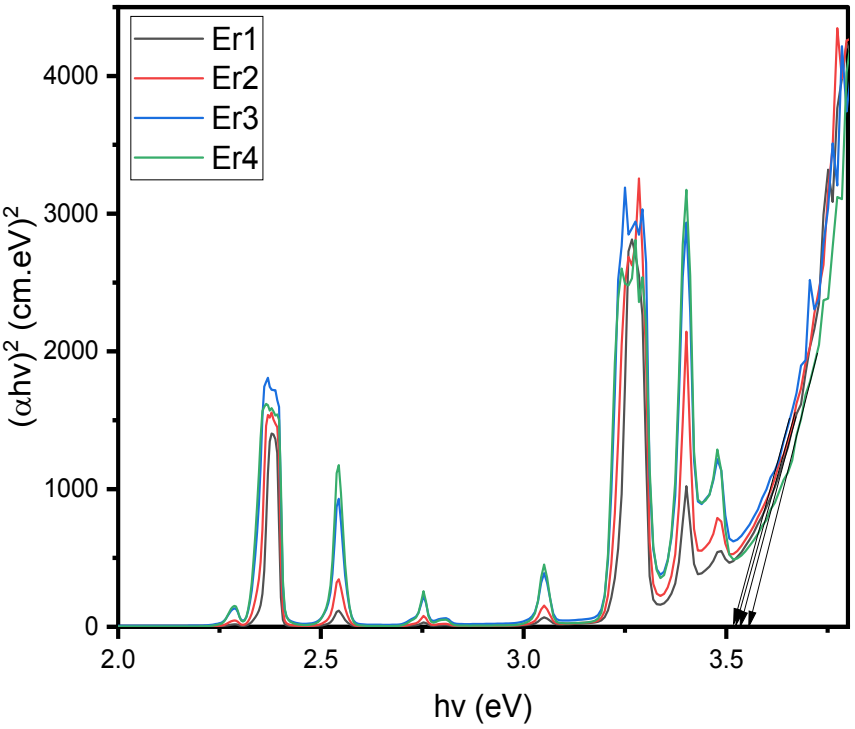

Figure 5: Indirect band gap for Er_2O_3-doped glass samples.

View Article Online
DOI: 10.1039/D6MA00313C

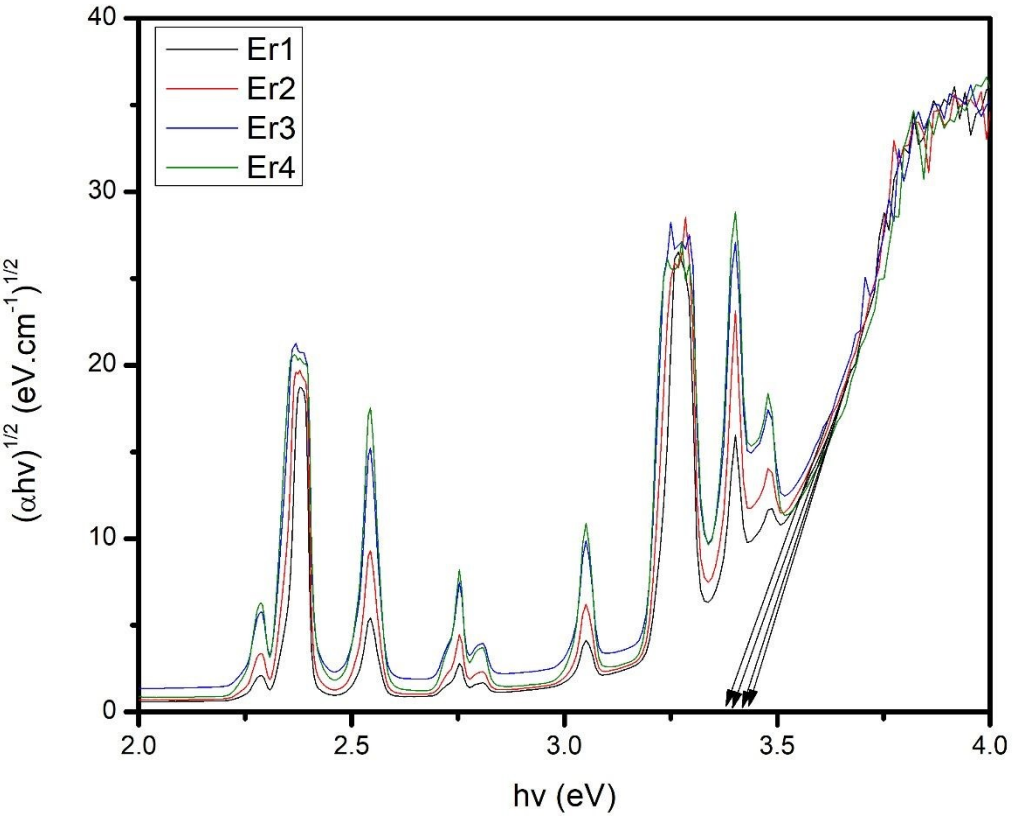

Figure 6: Direct band gap for Er_2O_3-doped glass samples.

View Article Online
DOI: 10.1039/D6MA00313C

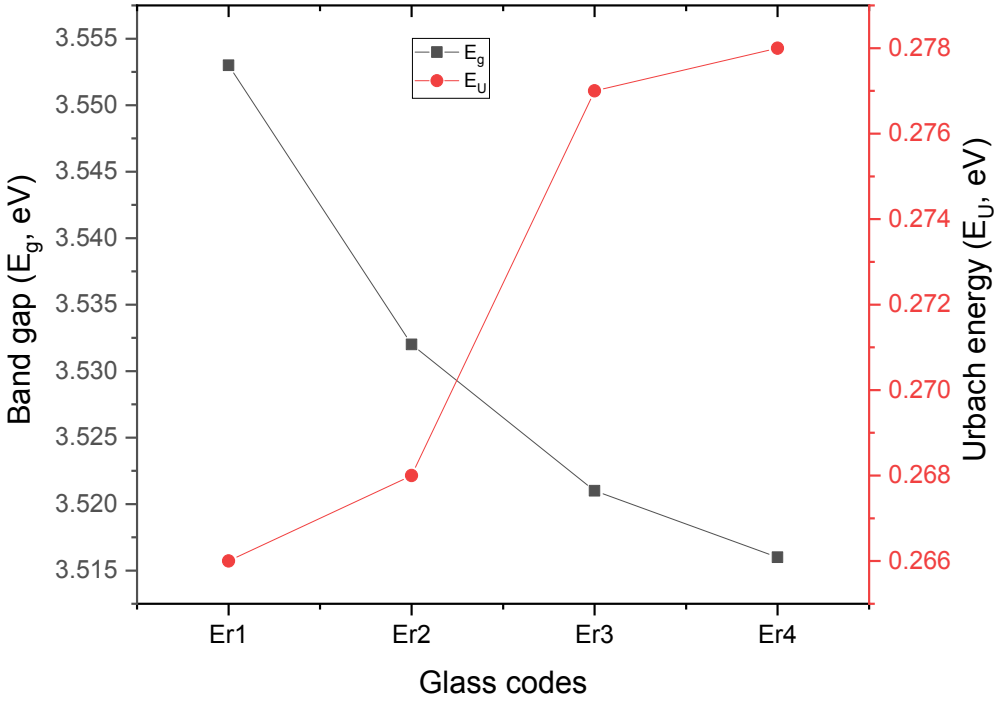

Figure 7: The relation band gap and Urbach energy for Er_2O_3-doped glass samples.

View Article Online
DOI: 10.1039/D6MA00313C

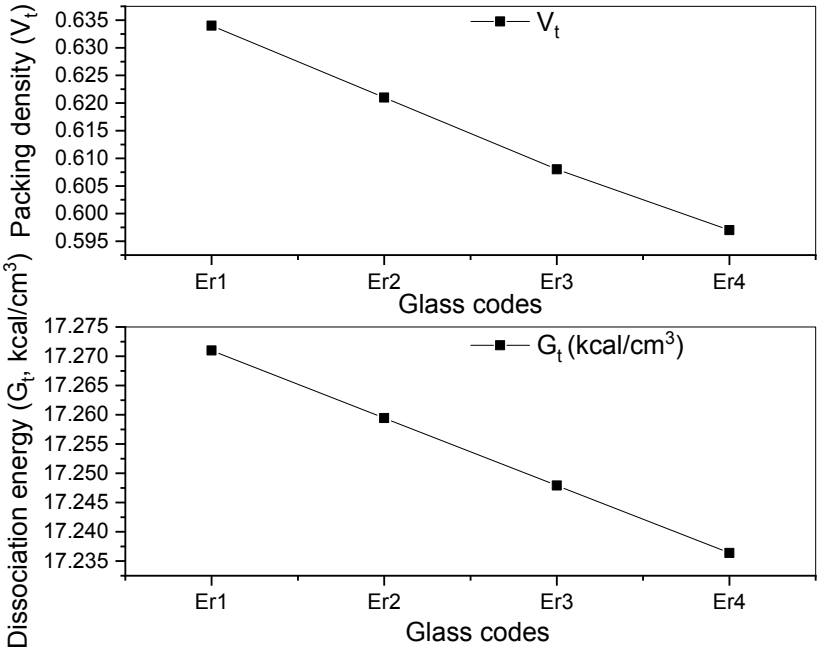

Figure 8: Er_2O_3-doped glass samples' dissociation energy and packing density.

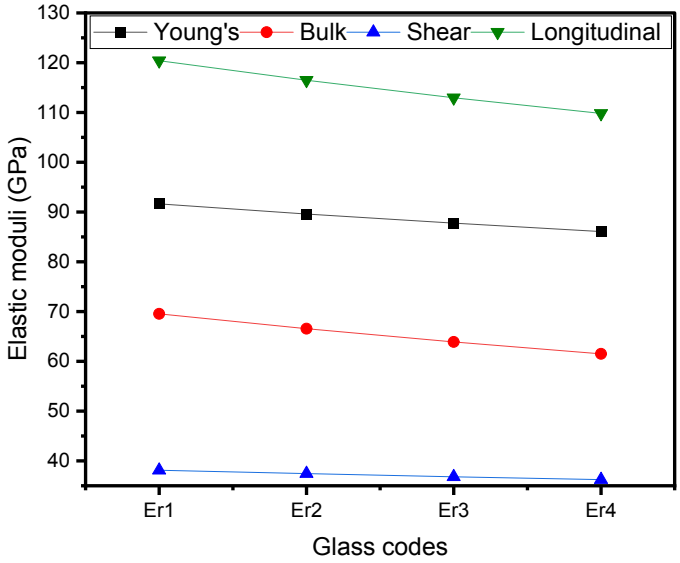

Figure 9: Elastic moduli for Er_2O_3-doped glass samples.

View Article Online
DOI: 10.1039/D6MA00313C

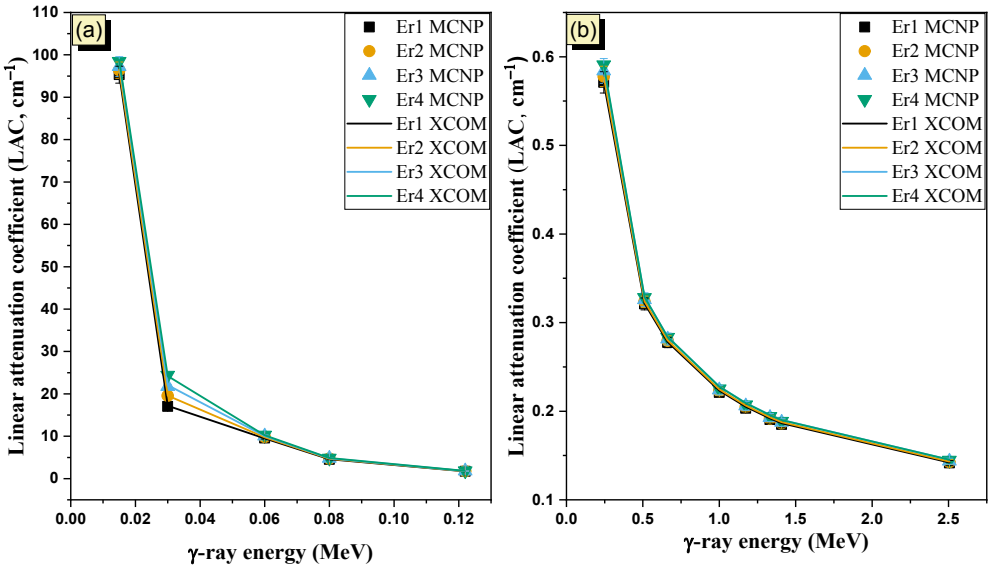

Figure 10: The linear attenuation coefficient (LAC) variation versus the γ-ray energies at (a) Photoelectric interval and (b) Compton scattering interval.

View Article Online
DOI: 10.1039/D6MA00313C

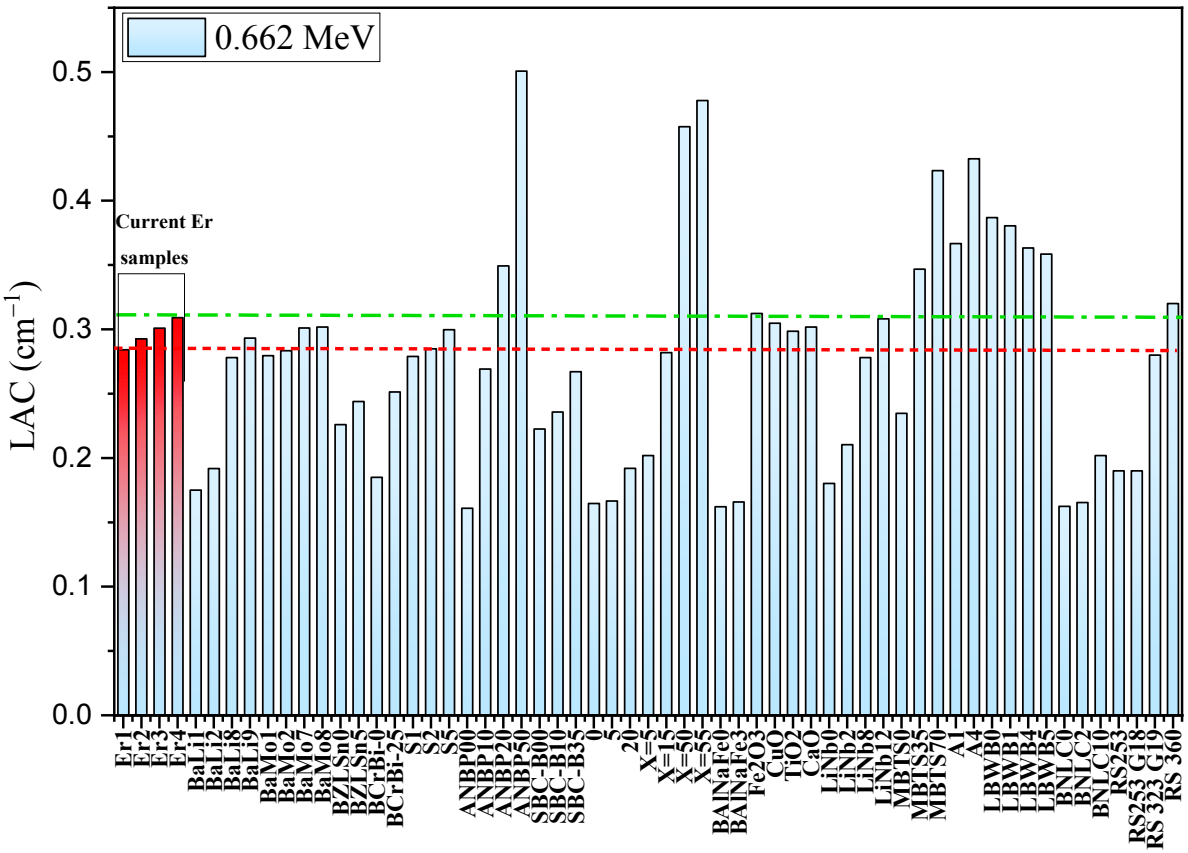

Figure 11: Comparison of the prepared Er glass samples' LAC versus those of commercial and similar glass samples from literature.

View Article Online
DOI: 10.1039/D6MA00313C

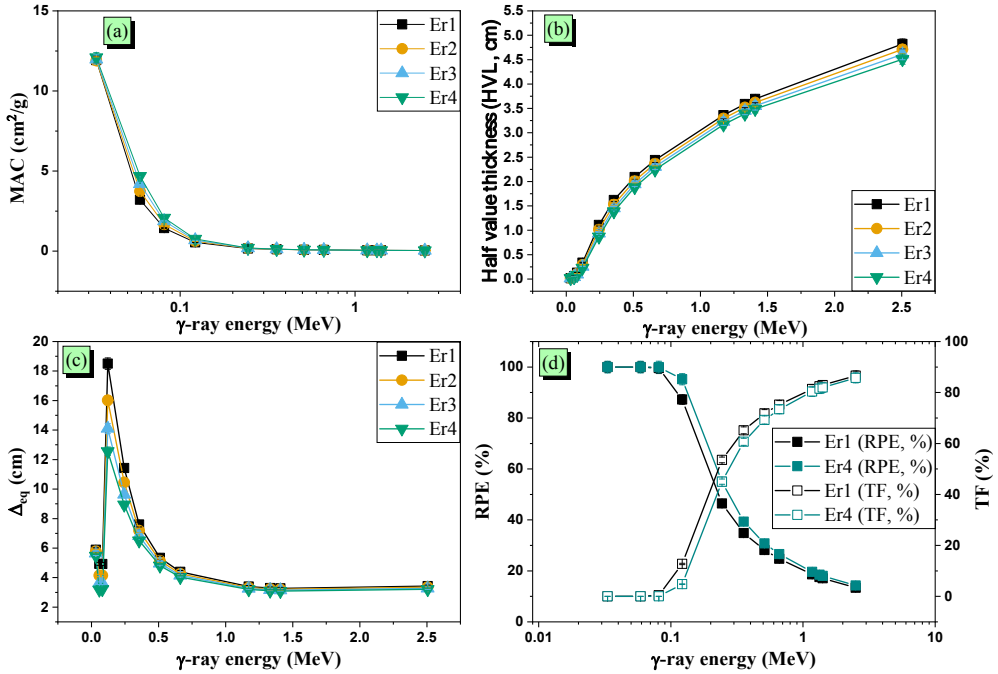

Figure 12: The γ-ray energy's influence on (a) mass attenuation coefficient (cm^2/g), (b) half-value thickness (cm), (c) sample thickness equivalent to 1 cm of lead (Δ_{eq}, cm), and (d) radiation protection efficiency (RPE, %) and transmission factor (TF, %) for the prepared Er glass samples.

View Article Online
DOI: 10.1039/D6MA00313C

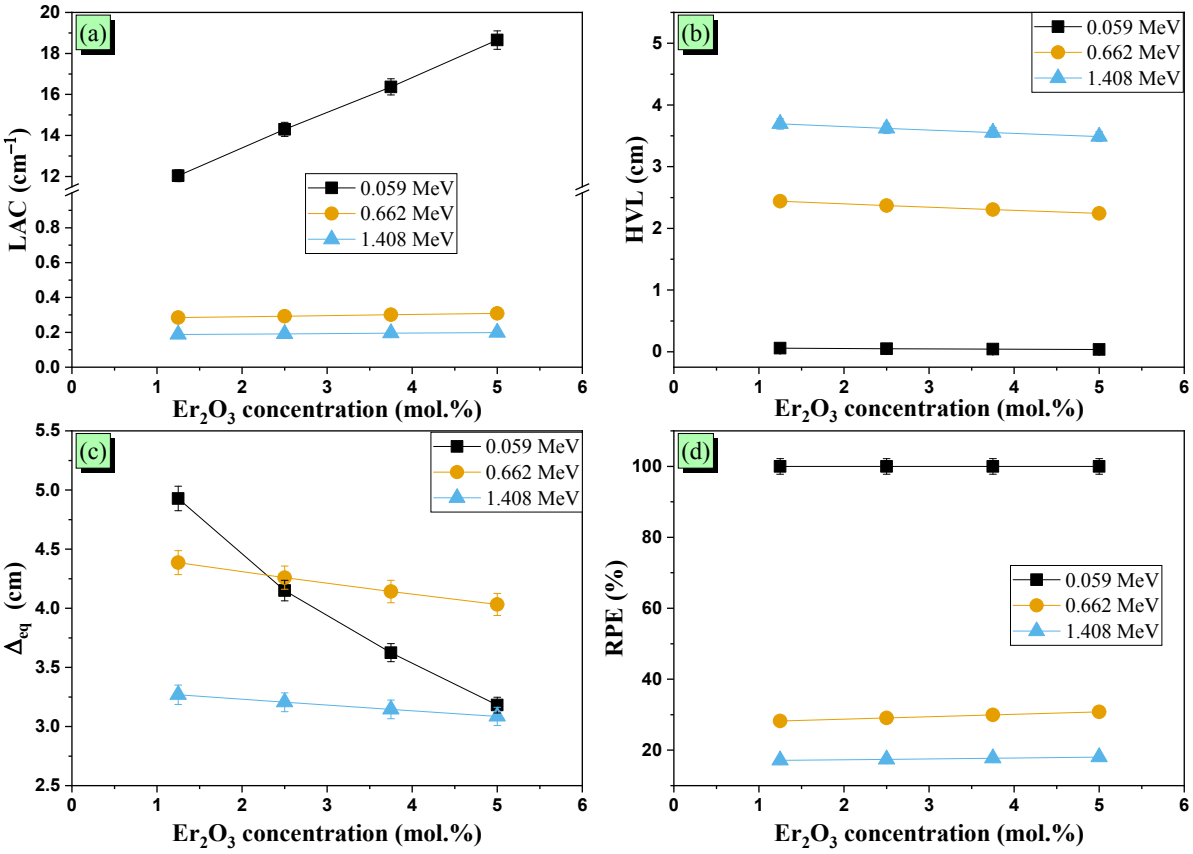

Figure 13: Variation of (a) LAC (cm^{-1}), (b) half-value thickness (HVL, cm), (c) sample thickness equivalent to 1 cm of lead (Δ_{eq}, cm), and (d) RPE (%) versus the Er_2O_3 concentrations in the prepared glass samples.

View Article Online
DOI: 10.1039/D6MA00313C

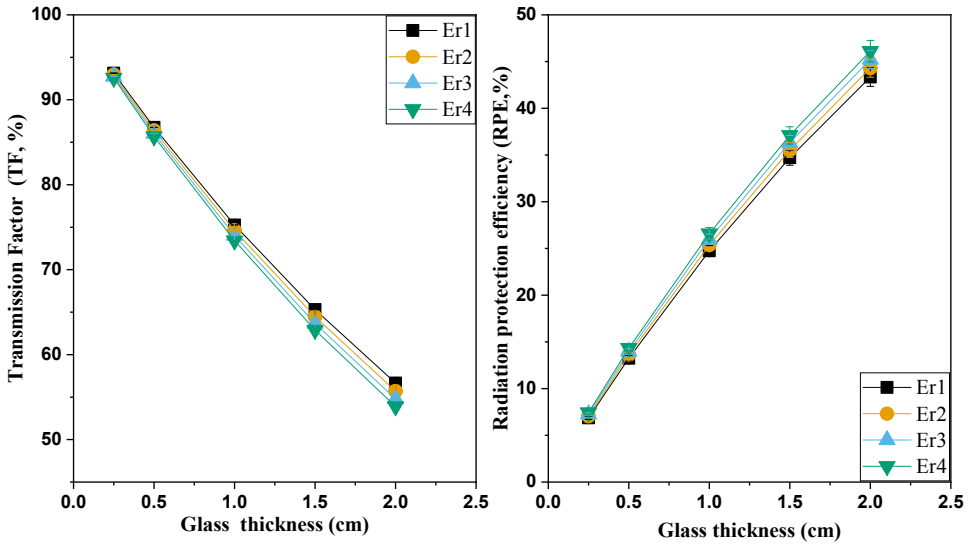

Figure 14: Variation of (a) TF (%) and (b) RPE (%) versus the glass thickness at 0.662 MeV.

View Article Online
DOI: 10.1039/D6MA00313C

The data that support the findings of this study will be available based on request